Applied Physics Letters

RESEARCH ARTICLE | JANUARY 25 2024

Using selective-area growth and selective-area etching on (−102) β-Ga_2O_3 substrates to fabricate plasma-damage-free vertical fins and trenches

Takayoshi Oshima ; Yuichi Oshima

Appl. Phys. Lett. 124, 042110 (2024)
https://doi.org/10.1063/5.0186319

Applied Physics Letters ARTICLE pubs.aip.org/aip/apl

Using selective-area growth and selective-area etching on (−102) β-Ga_2O_3 substrates to fabricate plasma-damage-free vertical fins and trenches

Cite as: Appl. Phys. Lett. **124**, 042110 (2024); doi: 10.1063/5.0186319
Submitted: 5 November 2023 · Accepted: 11 January 2024 ·
Published Online: 25 January 2024

View Online Export Citation CrossMark

Takayoshi Oshima[a] and Yuichi Oshima

AFFILIATIONS

Research Center for Electronic and Optical Materials, National Institute for Materials Science, Tsukuba, Ibaraki 305-0044, Japan

[a]Author to whom correspondence should be addressed: OSHIMA.Takayoshi@nims.go.jp

ABSTRACT

We have demonstrated selective-area growth and selective-area etching on SiO_2-masked (−102) β-Ga_2O_3 substrates using a HCl-based halide-vapor-phase epitaxy system that is capable of performing both growth and gas etching without plasma excitation. Since the surface of the (−102) substrate is perpendicular to the (100) plane, which has the lowest surface energy, we were able to use both methods to fabricate plasma-damage-free fins and trenches with (100)-faceted vertical sidewalls on windows striped along the [010] direction with high processing accuracy. Furthermore, since the [010] window direction is aligned parallel to the majority of dislocations and line-shaped voids in the substrate—which extend along the [010] direction and could potentially act as leakage paths—such crystal defects are unlikely to appear on the surfaces of the resulting fins and trenches. We believe that these selective-area growth/etching techniques can greatly accelerate research on, and the development of, β-Ga_2O_3-based vertical/lateral devices with fins or trenches.

The ultra-wide-bandgap semiconductor β-Ga_2O_3 has garnered considerable attention in recent years because it is expected to have a critical field strength as large as approximately 8 MV cm^{-1},[1] the widely controllable doping range of 10^{15}–10^{20} cm^{-3},[2] and high-quality wafers are available with the low defect densities of 10^3–10^5 cm^{-2}.[3] These properties all indicate that this material has significant potential for use in next-generation power semiconductors, following the footsteps of SiC and GaN. Because of such expectations, research on β-Ga_2O_3 has advanced in various areas, including the growth of bulk crystals, homo- and hetero-epitaxy, impurity doping, device design and processing, and related theoretical frameworks.[4]

Processing technologies that can be used to shape various structures on a wafer surface constitute one such area, which is indispensable for device manufacturing. In the β-Ga_2O_3 research community, plasma-based dry etching that utilizes chlorine-based chemistries is widely accepted as a proven process[5] for obtaining various structures, including mesas, fins, and trenches. They are used to define device regions and fabricate fin channels, recessed-gate structures, trench metal-oxide-semiconductor (trench MOS) structures, edge terminations, and so on. Utilizing such processed structures, fin field-effect transistors (FinFETs),[6–8] gate-recessed MOSFETs,[9] trench MOS Schottky barrier diodes (trench MOSSBDs),[10,11] trench MOSFETs,[12] and mesa-terminated SBDs[13,14] and PN diodes[15] have demonstrated improved device performance—for example, increased breakdown voltages and/or normally off operations—confirming the benefit of these structural effects. However, reactive ions in the plasma cause damage to the processed surfaces, degrading electrical properties of the devices such as the channel mobilities and transfer characteristics of FinFETs,[6,7] and the on-resistances of trench SBDs,[10] gate-recessed MOSFETs,[16] and mesa-terminated SBDs.[13] In order to recover from this damage and restore proper device performance, post-treatments like wet chemical etching[17–19] or annealing[16,19,20] are necessary. Thus, plasma etching is actually a two-step process that requires a damage-recovery procedure. In contrast, non-plasma-based wet and dry etching processes—such as metal-assisted chemical etching (MacEtch),[21] Ga-flux etching,[22] and hydrogen-environment anisotropic thermal etching (HEATE)[23]—have emerged as alternatives to plasma-based dry etching. These non-plasma techniques are quite promising, as evidenced by the facts that FinFETs formed using MacEtch show near-zero hysteresis in their gate-transfer characteristics,[24] that Ga-flux-etched recessed-gate MOSFETs have been produced with high drain currents and high transconductances,[25] and that trench MOSSBDs have been formed with near-ideal forward characteristics.[26]

In this context, we have recently demonstrated plasma-free selective-area growth (SAG) and selective-area etching (SAE) of commercially available (010) and (001) β-Ga_2O_3 substrates using a

laboratory-designed HCl-based halide-vapor-phase epitaxy (HVPE) system.[27–30] This HVPE system includes an HCl etching-gas line in addition to the growth-precursor lines that enable regulation of the balance between growth and etching. This enables growth on windows while suppressing nucleation on amorphous masks, thereby achieving SAG with perfect selectively. Alternatively, SAE can be performed in window areas using the HCl etching gas alone. Thus, this system can also be utilized as a halide-vapor-phase etching (HVPE) system. During both growth and etching, the sidewalls of the resulting structures are dominated by flat (100) facets owing to their high chemical stability, which can be attributed to the fact that they have the lowest surface energy density.[31,32] When the window direction is parallel to the (100) plane, the sidewalls consist exclusively of (100) facets, facilitating the production of high-aspect-ratio structures such as fins and trenches, as shown in Fig. 1. In particular, vertical fins and trenches can be created on (010) substrates due to the orthogonal relationship between the (100) and (010) planes. Nevertheless, a (010)-oriented substrate is unsuitable for vertical power-device applications because of its crystal defects. Since most line-shaped voids (also called nanopipes) and dislocations in the crystal exist along the [010] direction,[33–35] it is very likely for these crystal defects to appear on the surface of the resulting structures and act as leakage paths, causing premature breakdown.[36,37] Conversely, a (001) substrate can avoid such [010]-extended defect issues as the defects are parallel to the (001) plane and rarely surface on the substrate or the fins/trenches created thereon. However, the structures produced by the SAG or SAE on (001) substrates are inclined by 13.7° from the substrate normal because the face angle between the (100) and (001) planes is 103.7°. Such inclined fins and trenches are not suitable for vertical power-device applications, as the current and/or electric field is concentrated on either side of the structures. It is, therefore, necessary to consider the substrate orientation for implementation of the SAG and SAE methods in processing vertical power devices.

The $(\bar{1}02)$ plane is the optimal substrate orientation for using SAG and SAE to create fins/trenches with flat and vertical sidewalls that are suitable for vertical power-device applications. To produce fins/trenches with (100)-faceted vertical sidewalls, the substrate surface must be perpendicular to the (100) plane due to the dominance of (100) facets in the structures formed using SAG or SAE. To minimize the appearance of line-shaped voids and dislocations along the [010] direction on the surface, it is also necessary for the substrate to be oriented parallel to the [010] direction. To meet these two requirements, the substrate plane must be the $(\bar{1}02)$ plane, as shown in Fig. 1. We note that the $(\bar{1}02)$ plane can be set as the primary plane for edge-defined film-fed growth (EFG) because it is parallel to the [010] pulling direction.[38] This allows the fabrication of scalable wafers with high productivity, which can be comparable to the productivity achieved for (001) and $(\bar{2}01)$ wafers. In addition, prior to the present study, we verified that homoepitaxial growth is possible on $(\bar{1}02)$ substrates without misoriented domains, which is similar to the cases of (010) and (001) substrates.[39] Encouraged by these facts and expectations, we, therefore, performed experiments using SAG and SAE on $(\bar{1}02)$ substrates and investigated the resulting fin and trench structures.

We prepared SiO_2-masked $(\bar{1}02)$ β-Ga_2O_3 substrates as follows. $10 \times 15\,mm^2$ substrates with the $(\bar{1}02)$ orientation were manufactured by slicing, cutting, grinding, lapping, and chemically and mechanically polishing a Sn-doped ingot with (001) principal planes grown along the [010] direction using the EFG method (Novel Crystal Technology, Inc.). The $(\bar{1}02)$ substrates were monocrystalline, with highly crystalline quality that was comparable to those of commercially available (001) and (010) substrates. This is evidenced by the x-ray diffraction (XRD) results summarized in Fig. 2. As expected, we observed only a single peak in both the symmetric θ–2θ and skew-symmetric ϕ scans [Figs. 2(a) and 2(b), respectively]. The full-width at half maximum values of the ω rocking curves measured in the symmetric and skew-symmetric geometries were as narrow as 20–30 arc sec [Fig. 2(c)]. Prior to initiating the mask fabrication, we subjected the substrate surface to a meticulous cleaning process. This involved immersion in organic solvents, specifically acetone and isopropyl alcohol, followed by treatment with HF and a H_2SO_4/H_2O_2 blend. This step was crucial to ensure the complete removal of any residues from the chemical mechanical polishing slurry. Subsequently, the substrate surface was coated with a 0.10-μm-thick SiO_2 layer. This layer was applied using plasma-assisted chemical vapor deposition, utilizing tetraethoxysilane and O_2 as the source precursors. We then opened square-, radial-line-, and stripe-patterned windows in the SiO_2 layer using laser lithography, with buffered HF as the etchant. We removed the residual photoresist completely using organic solvents (acetone and isopropyl alcohol) and O_2 plasma. The square window was $100 \times 100\,\mu m^2$ in size. The radial pattern consisted of 36 window lines in 10° steps starting from [010]. The width of each window was 1.4 μm. We prepared two types of stripes: pattern A and pattern B. They were both parallel to the [010] direction, but they differed in the mask/window widths, which were 2.6/1.4 μm (pattern A) and 0.5/5.7 μm (pattern B).

We performed SAG and SAE using a laboratory-made HCl-based HVPE system similar to that employed in our previous experiments on (010)- and (001)-oriented substrates.[27–30] This system is equipped with a horizontal quartz reactor, which is divided into an upstream

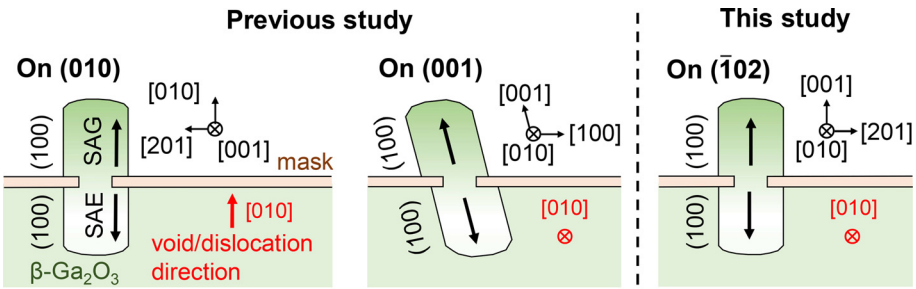

SAG: selective area growth, SAE: selective area etching

FIG. 1. (Two columns) Schematic cross sections of selective-area-grown and selective-area-etched structures on (010), (001), and $(\bar{1}02)$ substrates showing the directional relationships among the substrate planes, (100)-faceted sidewalls, and [010]-oriented propagation direction of the majority of voids and dislocations.

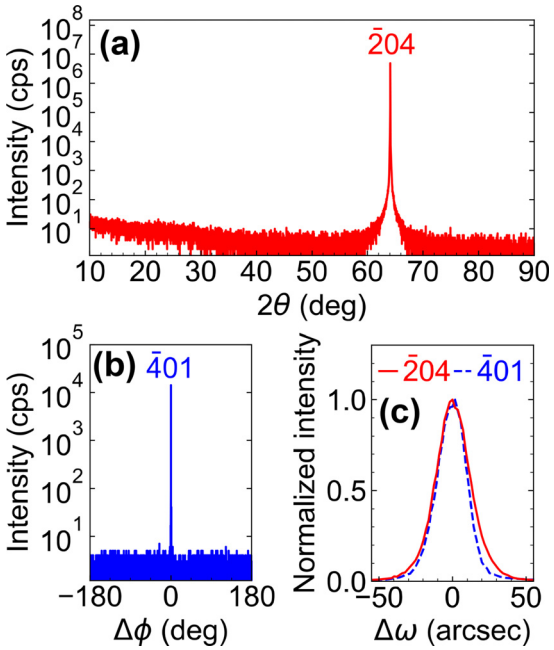

FIG. 2. (Single column) summary of the x-ray diffraction characterization of a ($\bar{1}02$)-oriented β-Ga_2O_3 substrate using Cu $K_{\alpha 1}$ radiation. (a) Symmetric θ–2θ scan pattern. (b) Skew-symmetric ϕ scan pattern at the tilt angle $\chi \sim 59.8°$. (c) The ω rocking curves of the $\bar{2}04$ and $\bar{4}01$ diffraction peaks corresponding to (a) and (b), respectively.

source zone and a downstream processing zone. In these zones, precursor and/or etching gases are introduced to a vertically oriented substrate. This substrate is mounted on a rotating holder for uniform exposure, as depicted in Fig. S1. For SAG, GaCl precursor was synthesized in the source zone at 822 °C using the chemical reaction between Ga metal (>99.999 99% pure) and HCl gas (>99.999% pure). Under the reaction conditions, the supplied HCl gas was completely consumed to generate an equimolar amount of GaCl gas. We then performed SAG by injecting the GaCl and O_2 (>99.999 95% pure) precursors, together with additional HCl etching gas, onto the surface of the SiO_2-masked ($\bar{1}02$) β-Ga_2O_3 substrate while heating the processing zone at 1038 °C for 15 min. It is necessary to supply the HCl etching gas to suppress parasitic gas-phase reactions and nucleation on the mask.[27,40] For SAE, we performed the etching by introducing the HCl etching gas onto the SiO_2-masked ($\bar{1}02$) substrate while heating the processing zone at 1038 °C for 10 min. For both SAG and SAE, the reactive gases were carried by purified N_2 gas (dew point < −110 °C) under atmospheric pressure (approximately 100 kPa), and we maintained the total gas flow through the reactor at 8 slm. The partial pressures of GaCl, O_2, and HCl (for etching purposes) were set at 0.125, 1.25, and 0.25 kPa in the case of SAG, and at 0, 0, and 62.5 Pa for SAE, respectively.

The substrates, post-growth, and etching were examined to determine surface compositions within 100×100 μm^2 window areas of both SAG and SAE substrates using Auger electron spectroscopy (AES). A bare ($\bar{1}02$) substrate, subjected to the cleaning process, was also analyzed for comparison. We examined the grown and etched structures using scanning electron microscopy (SEM). Additionally, we observed the cross sections of the structures using focused-ion-beam scanning electron microscopy (FIB–SEM), where we utilized carbon deposition as a protective layer against FIB milling. Furthermore, we viewed the atomic arrangement of the Ga atoms on the SAG β-Ga_2O_3 in the vicinity of the mask edge from the [010] direction using high-angle annular dark-field scanning transmission electron microscopy (HAADF–STEM) with an accelerating voltage of 200 kV.

We first assessed surface compositions following the SAG and SAE procedures. Figure 3 illustrates the typical AES spectra for the SAG, SAE, and the reference bare substrates. In all spectra, elements of Ga and O were present. C was also detected, likely due to hydrocarbon contaminants. Cl, however, was not detected within the analytical sensitivity of AES. The Ga/O atomic composition ratios for the SAG and SAE substrates, calculated using the relative sensitivity method, were 0.724 and 0.721, aligning with the reference value of 0.724. This consistency suggests that the SAG and SAE processes do not alter the Ga/O surface stoichiometry.

We then characterized the in-plane anisotropies of the SAG and SAE structures on the ($\bar{1}02$) substrates. Figures 4(a) and 4(b), respectively, show top-view SEM images of the SAG and SAE structures on the radial-patterned windows. We determined the lengths of the lateral overgrowth and under-etching perpendicular to the windows from these images by measuring the distances between the window edge and the end of the corresponding SAG fins and SAE trenches. We then plotted the acquired data in polar coordinates, as presented in Fig. 4(c). The results are similar to those observed on (001) substrates.[27,28] The lateral overgrowth and under etching were significantly reduced when the window directions were <010> because the corresponding sidewalls were the chemically most stable (100) facets. This is reflected in the polar plots, as the deepest dips occur in the [201] and [$\bar{2}0\bar{1}$] directions. Note that these directions are perpendicular to the (100) plane. Slight deviations from the <010> direction resulted in remarkable enhancements of the lateral growth and etching. For SAG, deviations of the window directions further from the <010> direction resulted in the deposition of polycrystals and/or the

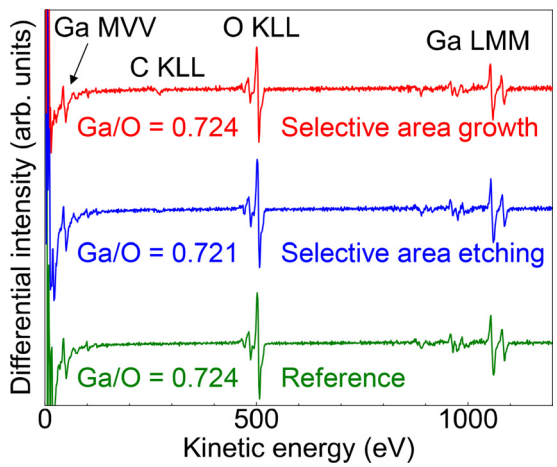

FIG. 3. (Single column) Auger electron spectra obtained from the 100×100 μm^2 window regions of the selective-area-grown and selective-area-etched samples. Additionally, it includes a spectrum from a cleaned bare ($\bar{1}02$) substrate, serving as a reference.

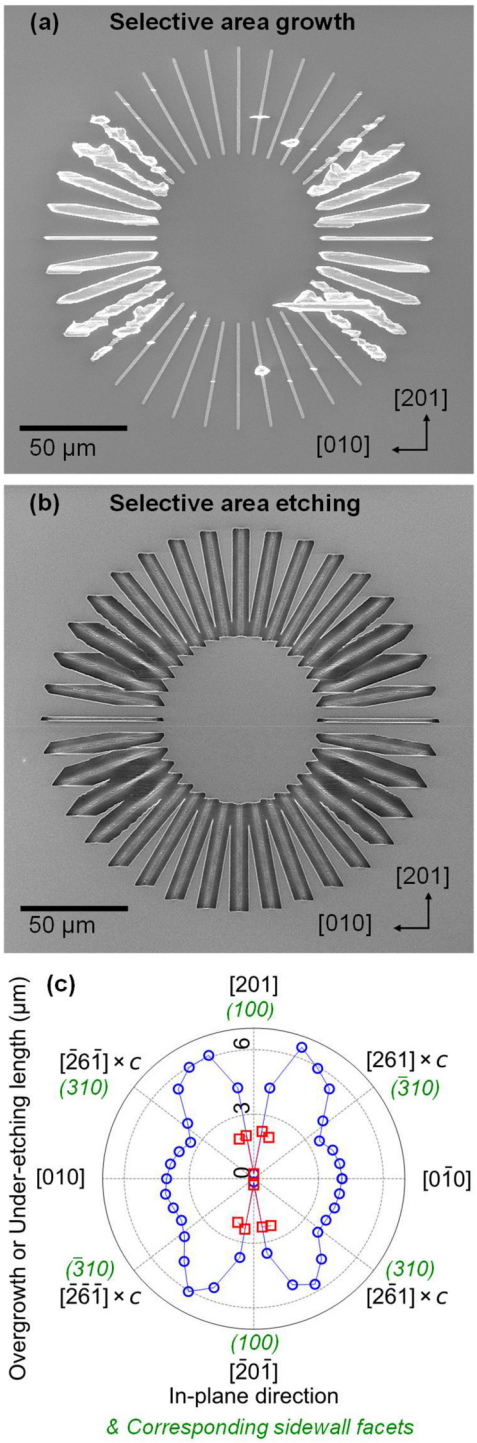

FIG. 4. (Single column) top-view scanning electron microscope images of (a) selective-area-grown and (b) selective-area-etched β-Ga_2O_3 on radial-line windows. (c) Polar plots of the lateral-overgrowth length (empty squares) and under-etching length (empty circles) measured from (a) and (b), respectively. The symbols "×" and "c" indicate the cross product of the given directions and the [001] direction. The solid lines connecting the data in (c) are guides to the eye.

absence of growth rather than in epitaxial growth of fins on the windows. Therefore, only the fins with (100) sidewalls survived, while those without were eliminated in the competition between growth and etching during SAG. For SAE, lateral etching was again suppressed as the deviation of the window directions increased. This resulted in small dips in the plots at the specific window directions where the sidewalls should be {310} facets. Consequently, the window direction should be [010] for the best controllability of the cross-sectional shape because the lateral size deviation of the fins/trenches from the mask width can be minimized.

We then investigated the SAG and SAE structures on the striped windows along the [010] direction using SEM, as shown in Fig. 5. Here, we used pattern A striped windows with a narrow window width to create both SAG fins and SAE trenches, while we used pattern B striped windows with a narrow mask width to fabricate SAE fins. In all cases, the overgrowth and under-etching lengths perpendicular to the windows were much smaller than the corresponding grown height and etched depth, respectively. This means that the fins and trenches were fabricated nearly according to the window and mask widths [Figs. 5(a), 5(f), and 5(k)]. In addition, vertical (100)-faceted sidewalls are clearly visible on both sides of the fins and trenches. In the SAG fins, the (100) sidewalls on the [$\bar{2}0\bar{1}$] side were shorter compared to those on the [201] side. This is attributed to the formation of a downward-sloping facet at the top surface [Figs. 5(b)–5(e)], identified as the ($\bar{2}01$) plane from subsequent cross-sectional analysis. Conversely, the (100) sidewalls on both sides were almost the same height in the SAE trenches and fins [Figs. 5(g)–5(j) and 5(l)–5(o)]. The etched bottom surfaces were relatively rough due to the presence of macro steps along the [010] direction. We also observed this roughness in the HCl-gas-etched bottom surface on the (001) substrates.[28]

Next, we examined the cross-sectional profiles of the fabricated SAG and SAE stripes along the [010] direction. Figures 6(a)–6(c) show tilted SEM images of the cross sections of the SAG and SAE stripes corresponding to those shown in Fig. 5. Figure 6(d) shows a schematic cross-sectional illustration with labeled facets for the SAG fins and SAE trenches on the pattern A masks. The SAG fins exhibited vertical (100)-faceted sidewalls and an inclined ($\bar{2}01$)-faceted top surface. The ($\bar{2}01$) facet's emergence is likely due to its relatively low surface energy density, second only to the (100) facet.[32] The structural aspect ratio—which we define to be the (100)-sidewall height divided by the lateral overgrowth or under-etching length—was 2.7 ([$\bar{2}0\bar{1}$] side)–6.7 ([201] side). It is important to note that there were small bumps on both sides of the (100) sidewalls of the fins due to the formation of twin domains during the lateral overgrowth, which we discuss later. Conversely, the SAE trenches and fins consisted of vertical (100)-faceted sidewalls and a relatively rough bottom surface. Note that the (100) sidewall on the [$\bar{2}0\bar{1}$] side was not perfectly vertical but slightly curved. Moreover, the under-etching length on the [$\bar{2}0\bar{1}$] side was a little bit longer than that of the sidewall on the [201] side. The detailed reason for this left–right asymmetry of the sidewalls is unclear at the moment, but it must be related to the anisotropy of the monoclinic structure. Optimization of the etching parameters—such as the processing temperature and HCl partial pressure[30]—may flatten the (100) sidewalls on the [$\bar{2}0\bar{1}$] side because the (100) and ($\bar{1}$ 00) planes that correspond to the opposing sidewalls are crystallographically equivalent. The structural aspect ratio was 7.9 ([201] side)–11.2 ([$\bar{2}0\bar{1}$] side), which is higher than the corresponding values for the SAG structures.

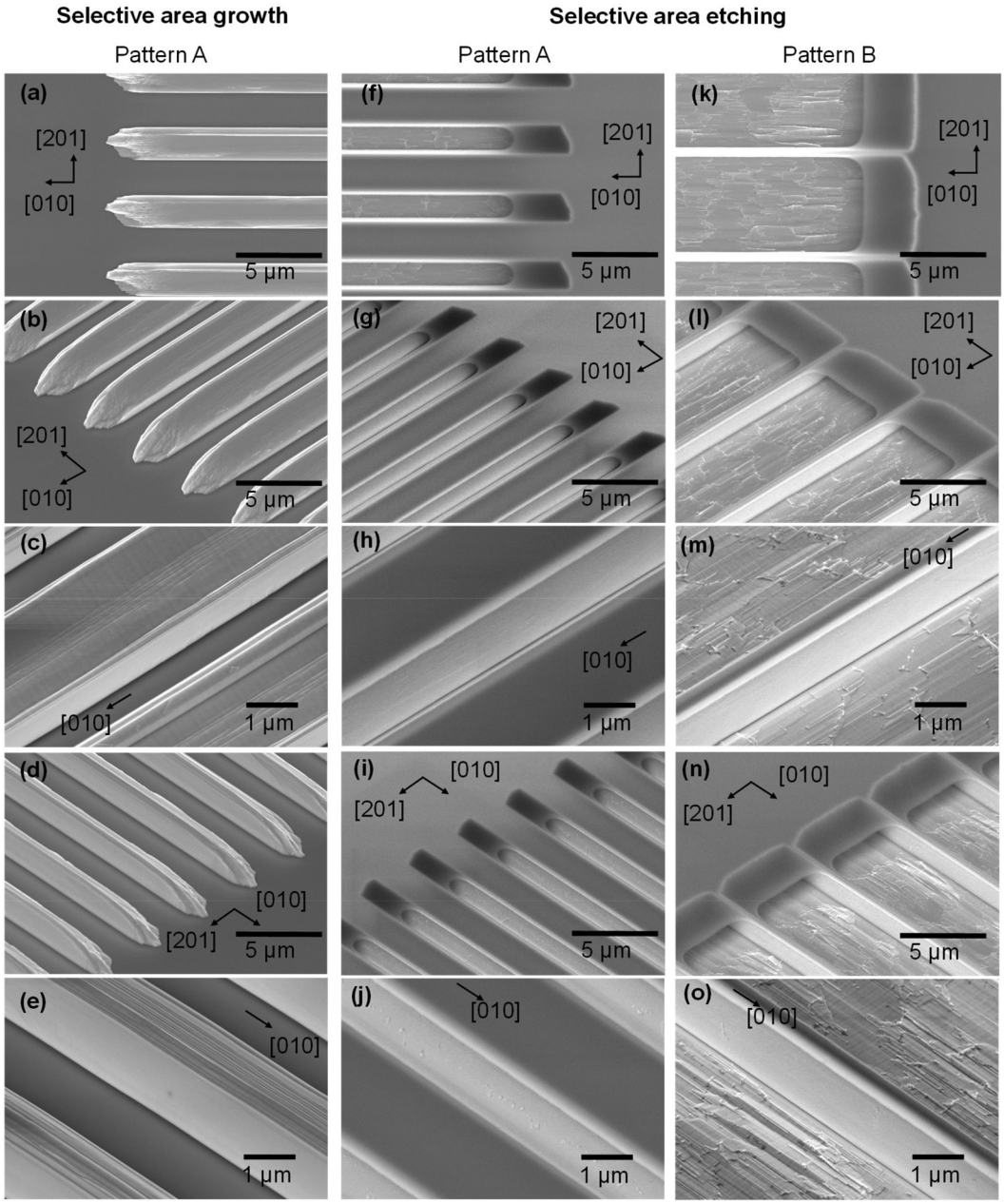

FIG. 5. (Two columns) top- and tilted-view scanning electron microscope images (at angles of 0° and 50° relative to the sample normal, respectively), of the selective-area-grown fins on the stripe mask of (a)–(e) pattern A and of the selective-area-etched trenches under the stripe masks of (f)–(j) pattern A and (k)–(o) pattern B.

Finally, we examined the atomic arrangements of the overgrown region of the SAG β-Ga_2O_3 using STEM, as shown in Fig. 7. It is highly probable for twinning to occur during lateral overgrowth on the (100) sidewalls because homoepitaxial growth on (100) β-Ga_2O_3 substrates without miscut angle forms twin lamellae due to the double positioning of the adatoms on the (100) plane.[41] Figures 7(a) and 7(b) display HAADF–STEM images in the vicinity of the mask edge, in which the comparatively heavy Ga atoms are visible as white dots. We observed a single periodic arrangement of Ga atoms in the substrate region and in the SAG region above the window, which is consistent with the result from homoepitaxy on $(\bar{1}02)$ β-Ga_2O_3 substrates.[39] We found a twin domain in the lateral-overgrown region above the mask alongside a coherent boundary stemming from the mask edge, as evidenced by the twin symmetry of the fast Fourier transformed images of the two domain regions that cross the boundary [Figs. 7(c) and 7(d)]. These findings indicate that the twinning was

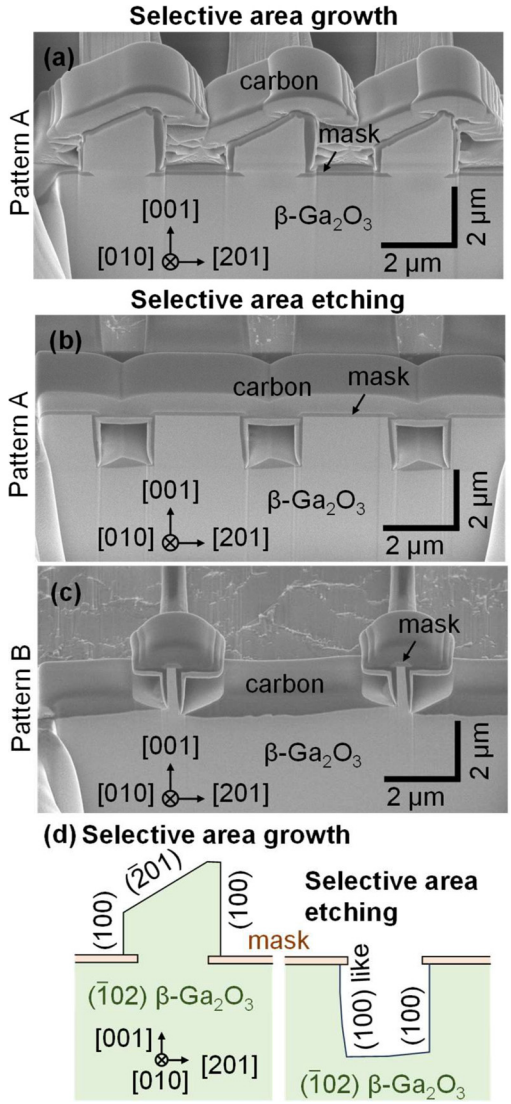

FIG. 6. (Single column) (a)–(c) 54°-tilted-view scanning electron microscope images of the cross-sectional structures of selective-area-grown fins and selective-area-etched trenches. The fins in panel (a) correspond to Figs. 5(a)–5(e) (pattern A). The trenches in panels (b) and (c) correspond to Figs. 5(f)–5(j) (pattern A) and Figs. 5(k)–5(o) (pattern B), respectively. (d) Schematic cross sections of (a) and (b).

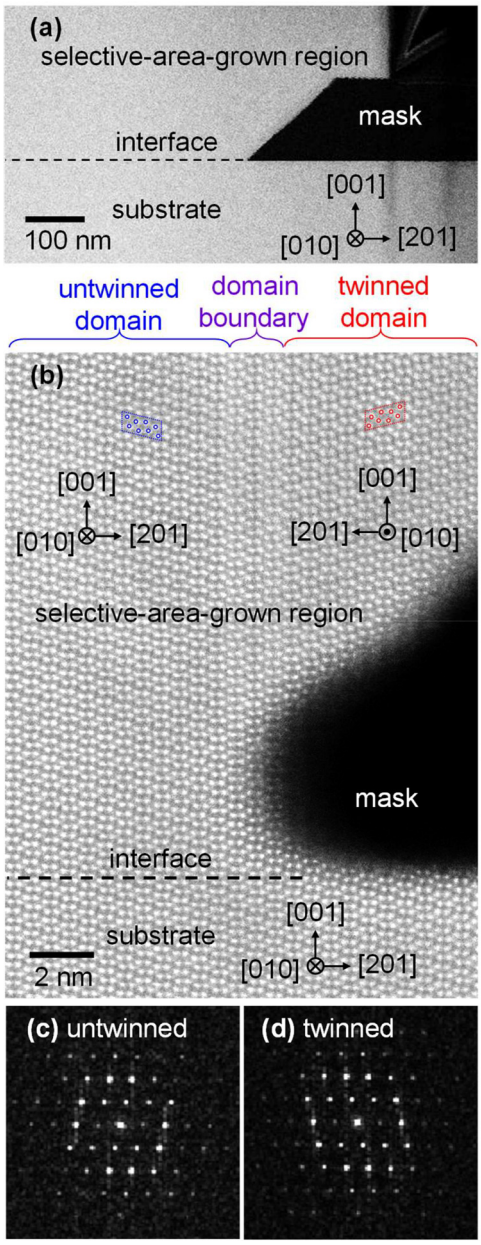

FIG. 7. (Single column) high-angle annular dark-field scanning transmission electron microscope images around the mask edge of a selective-area-grown β-Ga_2O_3 region taken at (a) low and (b) high magnifications. In (b), the small empty circles surrounded by blue and red dashed parallelograms represent Ga atoms in unit cells in the untwinned and twinned domains, respectively. The bottom panels show fast Fourier transformed images of (c) the untwinned and (d) the twinned domain regions.

caused by the same mechanism as that occurring during homoepitaxial growth on (100) substrates. The twin formation is anticipated not only for the ($\bar{1}02$) substrates but also on the SAG sidewalls for the (010) and (001) substrates, in line with this mechanism. Therefore, it is crucial to consider the presence of twin domains located proximate to the (100) sidewall surfaces when employing SAG structures for devices.

In summary, we have explored the potential of SAG and SAE using HVPE as one-step plasma-free processes for β-Ga_2O_3. By utilizing ($\bar{1}02$)-oriented substrates, which are perpendicular to the (100) plane and parallel to the [010] direction, we have been able to use SAG and SAE to fabricate high-aspect-ratio fins and trenches with (100)-faceted vertical sidewalls along the [010] direction. In addition to being free of plasma damage, these structures can also prevent line-shaped voids and dislocations that extend in the [010] direction from appearing on their surfaces, making them suitable for both vertical and lateral device applications. However, we have also found that SAG

inevitably causes twinning in the lateral-overgrown region of the (100) sidewalls. This occurs because the lateral growth is virtually the same as homoepitaxial growth on (100) substrates. Therefore, SAE is more promising than SAG for practical device applications.

See the supplementary material for the schematics illustrating the gas flows in the HVPE system (Fig. S1).

The authors thank T. Harada of the National Institute for Materials Science regarding XRD characterization and Y. Yao of the Japan Fine Ceramics Center for valuable discussions on dislocations in β-Ga_2O_3. This research was partially funded by the TEPCO Memorial Foundation and supported by the Advanced Research Infrastructure for Materials and Nanotechnology in Japan (ARIM) of the Ministry of Education, Culture, Sports, Science and Technology (MEXT), Proposal No. JPMXP1223 NM5073.

AUTHOR DECLARATIONS

Conflict of Interest

The authors have no conflicts to disclose.

Author Contributions

Takayoshi Oshima: Conceptualization (lead); Data curation (lead); Methodology (equal); Writing – original draft (lead). **Yuichi Oshima:** Conceptualization (supporting); Methodology (equal); Writing – review & editing (lead).

DATA AVAILABILITY

The data that support the findings of this study are available from the corresponding author upon reasonable request.

REFERENCES

[1]M. Higashiwaki, K. Sasaki, A. Kuramata, T. Masui, and S. Yamakoshi, Appl. Phys. Lett. **100**, 013504 (2012).
[2]J. Zhang, J. Shi, D.-C. Qi, L. Chen, and K. H. L. Zhang, APL Mater. **8**, 020906 (2020).
[3]O. Ueda, M. Kasu, and H. Yamaguchi, Jpn. J. Appl. Phys., Part 1 **61**, 050101 (2022).
[4]A. J. Green, J. Speck, G. Xing, P. Moens, F. Allerstam, K. Gumaelius, T. Neyer, A. Arias-Purdue, V. Mehrotra, A. Kuramata, K. Sasaki, S. Watanabe, K. Koshi, J. Blevins, O. Bierwagen, S. Krishnamoorthy, K. Leedy, A. R. Arehart, A. T. Neal, S. Mou, S. A. Ringel, A. Kumar, A. Sharma, K. Ghosh, U. Singisetti, W. Li, K. Chabak, K. Liddy, A. Islam, S. Rajan, S. Graham, S. Choi, Z. Cheng, and M. Higashiwaki, APL Mater. **10**, 029201 (2022).
[5]R. Khanna, K. Bevlin, D. Geerpuram, J. Yang, F. Ren, and S. Pearton, *Gallium Oxide* (Elsevier, 2019), pp. 263–285.
[6]K. D. Chabak, N. Moser, A. J. Green, D. E. Walker, S. E. Tetlak, E. Heller, A. Crespo, R. Fitch, J. P. McCandless, K. Leedy, M. Baldini, G. Wagner, Z. Galazka, X. Li, and G. Jessen, Appl. Phys. Lett. **109**, 213501 (2016).
[7]Z. Hu, K. Nomoto, W. Li, Z. Zhang, N. Tanen, Q. T. Thieu, K. Sasaki, A. Kuramata, T. Nakamura, D. Jena, and H. G. Xing, Appl. Phys. Lett. **113**, 122103 (2018).
[8]W. Li, K. Nomoto, Z. Hu, T. Nakamura, D. Jena, and H. G. Xing, *2019 IEEE Int. Electron Devices Meet.* (IEEE, 2019).
[9]K. D. Chabak, J. P. McCandless, N. A. Moser, A. J. Green, K. Mahalingam, A. Crespo, N. Hendricks, B. M. Howe, S. E. Tetlak, K. Leedy, R. C. Fitch, D. Wakimoto, K. Sasaki, A. Kuramata, and G. H. Jessen, IEEE Electron Device Lett. **39**, 67 (2018).
[10]W. Li, K. Nomoto, Z. Hu, D. Jena, and H. G. Xing, IEEE Trans. Electron Devices **68**, 2420 (2021).
[11]F. Otsuka, H. Miyamoto, A. Takatsuka, S. Kunori, K. Sasaki, and A. Kuramata, Appl. Phys. Express **15**, 016501 (2022).
[12]Y. Ma, X. Zhou, W. Tang, X. Zhang, G. Xu, L. Zhang, T. Chen, S. Dai, C. Bian, B. Li, Z. Zeng, and S. Long, IEEE Electron Device Lett. **44**, 384 (2023).
[13]S. Dhara, N. K. Kalarickal, A. Dheenan, C. Joishi, and S. Rajan, Appl. Phys. Lett. **121**, 203501 (2022).
[14]H. Chen, H. Wang, and K. Sheng, IEEE Electron Device Lett. **44**, 21 (2023).
[15]K. Danno, M. Kado, T. Hara, T. Takasugi, H. Yamano, Y. Umetani, and T. Shoji, Jpn. J. Appl. Phys., Part 1 **62**, SF1007 (2023).
[16]S. Sharma, L. Meng, A. F. M. A. U. Bhuiyan, Z. Feng, D. Eason, H. Zhao, and U. Singisetti, IEEE Electron Device Lett. **43**, 2029 (2022).
[17]Y. Zhang, A. Mauze, F. Alema, A. Osinsky, and J. S. Speck, Appl. Phys. Express **12**, 044005 (2019).
[18]H.-K. Lee, H.-J. Yun, K.-H. Shim, H.-G. Park, T.-H. Jang, S.-N. Lee, and C.-J. Choi, Appl. Surf. Sci. **506**, 144673 (2020).
[19]Z. Wang, X. Yu, H. Gong, T. Hu, Y. Zhang, X. Ji, F. Ren, S. Gu, Y. Zheng, R. Zhang, A. Y. Kuznetsov, and J. Ye, J. Phys. Chem. Lett. **13**, 7094 (2022).
[20]J. Yang, F. Ren, R. Khanna, K. Bevlin, D. Geerpuram, L.-C. Tung, J. Lin, H. Jiang, J. Lee, E. Flitsiyan, L. Chernyak, S. J. Pearton, and A. Kuramata, J. Vac. Sci. Technol., B **35**, 051201 (2017).
[21]H. Huang, M. Kim, X. Zhan, K. Chabak, J. D. Kim, A. Kvit, D. Liu, Z. Ma, J.-M. Zuo, and X. Li, ACS Nano **13**, 8784 (2019).
[22]N. K. Kalarickal, A. Fiedler, S. Dhara, H.-L. Huang, A. F. M. A. U. Bhuiyan, M. W. Rahman, T. Kim, Z. Xia, Z. J. Eddine, A. Dheenan, M. Brenner, H. Zhao, J. Hwang, and S. Rajan, Appl. Phys. Lett. **119**, 123503 (2021).
[23]Y. Yamazaki, M. Tomoaki, A. Takeki, and A. Kikuchi, in 4th International Workshop on Gallium Oxide and Related Materials, 2022.
[24]H.-C. Huang, Z. Ren, A. F. M. Anhar Uddin Bhuiyan, Z. Feng, Z. Yang, X. Luo, A. Q. Huang, A. Green, K. Chabak, H. Zhao, and X. Li, Appl. Phys. Lett. **121**, 052102 (2022).
[25]N. K. Kalarickal, A. Dheenan, J. F. McGlone, S. Dhara, M. Brenner, S. A. Ringel, and S. Rajan, Appl. Phys. Lett. **122**, 113506 (2023).
[26]S. Dhara, N. K. Kalarickal, A. Dheenan, S. I. Rahman, C. Joishi, and S. Rajan, Appl. Phys. Lett. **123**, 023503 (2023).
[27]T. Oshima and Y. Oshima, Appl. Phys. Express **15**, 075503 (2022).
[28]T. Oshima and Y. Oshima, Appl. Phys. Lett. **122**, 162102 (2023).
[29]T. Oshima and Y. Oshima, Appl. Phys. Express **16**, 066501 (2023).
[30]Y. Oshima and T. Oshima, Jpn. J. Appl. Phys., Part 1 **62**, 080901 (2023).
[31]S. Mu, M. Wang, H. Peelaers, and C. G. Van de Walle, APL Mater. **8**, 091105 (2020).
[32]R. Schewski, K. Lion, A. Fiedler, C. Wouters, A. Popp, S. V. Levchenko, T. Schulz, M. Schmidbauer, S. Bin Anooz, R. Grüneberg, Z. Galazka, G. Wagner, K. Irmscher, M. Scheffler, C. Draxl, and M. Albrecht, APL Mater. **7**, 022515 (2019).
[33]O. Ueda, N. Ikenaga, K. Koshi, K. Iizuka, A. Kuramata, K. Hanada, T. Moribayashi, S. Yamakoshi, and M. Kasu, Jpn. J. Appl. Phys.,Part 1 **55**, 1202BD (2016).
[34]E. Ohba, T. Kobayashi, M. Kado, and K. Hoshikawa, Jpn. J. Appl. Phys., Part 1 **55**, 1202BF (2016).
[35]Y. Yao, Y. Tsusaka, K. Sasaki, A. Kuramata, Y. Sugawara, and Y. Ishikawa, Appl. Phys. Lett. **121**, 012105 (2022).
[36]M. Kasu, T. Oshima, K. Hanada, T. Moribayashi, A. Hashiguchi, T. Oishi, K. Koshi, K. Sasaki, A. Kuramata, and O. Ueda, Jpn. J. Appl. Phys., Part 1 **56**, 091101 (2017).
[37]Y. Yao, D. Wakimoto, H. Miyamoto, K. Sasaki, A. Kuramata, K. Hirano, Y. Sugawara, and Y. Ishikawa, Scr. Mater. **226**, 115216 (2023).
[38]A. Kuramata, K. Koshi, S. Watanabe, Y. Yamaoka, T. Masui, and S. Yamakoshi, Jpn. J. Appl. Phys, Part 1 **55**, 1202A2 (2016).
[39]Y. Oshima and T. Oshima, Semicond. Sci. Technol. **38**, 105003 (2023).
[40]Y. Oshima, K. Kawara, T. Oshima, M. Okigawa, and T. Shinohe, Semicond. Sci. Technol. **35**, 055022 (2020).
[41]R. Schewski, M. Baldini, K. Irmscher, A. Fiedler, T. Markurt, B. Neuschulz, T. Remmele, T. Schulz, G. Wagner, Z. Galazka, and M. Albrecht, J. Appl. Phys. **120**, 225308 (2016).